Journal of Microscopy

Journal of Microscopy, Vol. 262, Issue 3 2016, pp. 316–325 doi: 10.1111/jmi.12367

Received 22 September 2015; accepted 19 November 2015

Far-reaching geometrical artefacts due to thermal decomposition of polymeric coatings around focused ion beam milled pigment particles

K. RYKACZEWSKI*, D.G. MIERITZ†, M. LIU*, Y. MA*, E.B. IEZZI‡, X. SUN*, L.P. WANG*, K.N. SOLANKI*, D.-K. SEO† & R.Y. WANG*

**School for Engineering of Transport, Matter and Energy, Arizona State University, Tempe, Arizona, U.S.A.*

†*Department of Chemistry and Biochemistry, Arizona State University, Tempe, Arizona, U.S.A.*

‡*Naval Research Laboratory, Chemistry Division, Washington, DC, U.S.A.*

Key words. FIB-SEM, heating artefacts, paints, pigments.

Summary

Focused ion beam and scanning electron microscope (FIB-SEM) instruments are extensively used to characterize nanoscale composition of composite materials, however, their application to analysis of organic corrosion barrier coatings has been limited. The primary concern that arises with use of FIB to mill organic materials is the possibility of severe thermal damage that occurs in close proximity to the ion beam impact. Recent research has shown that such localized artefacts can be mitigated for a number of polymers through cryogenic cooling of the sample as well as low current milling and intelligent ion beam control. Here we report unexpected nonlocalized artefacts that occur during FIB milling of composite organic coatings with pigment particles. Specifically, we show that FIB milling of pigmented polysiloxane coating can lead to formation of multiple microscopic voids within the substrate as far as 5 μm away from the ion beam impact. We use further experimentation and modelling to show that void formation occurs via ion beam heating of the pigment particles that leads to decomposition and vaporization of the surrounding polysiloxane. We also identify FIB milling conditions that mitigate this issue.

Introduction

Dual beam instruments that combine focused ion beam with a scanning electron microscope (FIB-SEM) are extensively used for characterization of various materials ranging from semiconductors to biological tissue (Stevie *et al.*, 2005; Volkert & Minor, 2007; Bassim *et al.*, 2014), but have not been applied to analysis of organic corrosion barrier coatings. In the past, FIB-SEM has been used for site specific cross sectioning and/or lamella extraction for transmission electron microscope imaging (White *et al.*, 2001; Lins *et al.*, 2002; Loos *et al.*, 2002; Beach *et al.*, 2005; Brunner *et al.*, 2006, 2008; Brostow *et al.*, 2007; Kawahara *et al.*, 2008; Martínez *et al.*, 2008; Wong *et al.*, 2010; Firpo *et al.*, 2015; Qin *et al.*, 2015), destructive tomography (Kato *et al.*, 2007; Lin *et al.*, 2012; Olea-Mejía *et al.*, 2012) and nanofabrication (Aubry *et al.*, 2002; Niihara *et al.*, 2005; Lee *et al.*, 2012; Schmied *et al.*, 2012; Orthacker *et al.*, 2014; Schmied *et al.*, 2014) of polymers and polymeric composites. Out of these examples, only a few studies have been dedicated to characterization of pristine organic coatings and paints (Lins *et al.*, 2002; Brunner *et al.*, 2006, 2008; Brostow *et al.*, 2007; Lin *et al.*, 2012; Chen *et al.*, 2013; Doutre *et al.*, 2014). With respect to corrosion barrier coatings, FIB-SEM characterization can provide quantitative nanoscale information about three dimensional distributions of pigment particles and pores in both pristine as well as corroded samples. Both of these physical features strongly impact resistance of the coatings to penetration by water and dissolved ions (Nguyen *et al.*, 1996; Lambourne & Strivens, 1999; Van der Wel & Adan, 1999; Chen *et al.*, 2013, 2014), but their influence is typically quantified in total or effective terms using macroscopic techniques (Nguyen *et al.*, 1995; Linossier *et al.*, 1997; Bierwagen *et al.*, 2003). Chen and co-workers recently measured three dimensional distribution of aluminium flakes dispersed in epoxy using serial block-face SEM imaging and x-ray tomography and used this data to theoretically predict resistance of the coating to penetration by corrosive ions (Chen *et al.*, 2013). In contrast to mechanical slicing using a microtome, FIB can be used to mill a smooth cross section of a pigmented paint without risk of artefacts arising from heterogeneous mechanical properties of the sample (e.g. dislodging of particles by the microtome blade). Another advantage of using FIB-SEM over serial block-face and x-ray tomography of organic coatings is minimal sample preparation. Specifically, cross sectioning and destructive tomography can be performed at any location of a coated substrate before and after corroding.

Authors D.G. Mieritz and M. Liu contributed equally to this script.

Correspondence to: K. Rykaczewski, School for Engineering of Transport, Matter and Energy, Arizona State University, Tempe, AZ 85287, U.S.A. Tel. 480-727-2050; e-mail: konradr@asu.edu

The primary concern that arises when using FIB-SEM to characterize a polymeric sample is the possibility of severe damage induced by ion beam heating of the sample (Volkert & Minor, 2007; Kim *et al.*, 2011; Bassim *et al.*, 2012). To date thermal damage stemming from significant temperature rise in vicinity of the ion beam impact has been described. For a material with thermal conductivity k, the maximum temperature increase due to impact of an ion beam with power $\dot{q}$ and diameter d_b can be estimated as $\Delta T \sim 2\dot{q}/\pi d_b k$ (Vineyard, 1976; Volkert & Minor, 2007; Kim *et al.*, 2011; Das *et al.*, 2015). For typical polymer with $k \sim 0.1$ W Km^{-1}, impact of a modern focused gallium ion beam with $2\dot{q}/d_b$ up to 1000 W m^{-1} can cause a temperature increase greater than 3000 K (Kim *et al.*, 2011). Naturally, polymers decompose and partially volatilize prior to reaching such temperatures. However, this process can introduce molecular scale changes that are detectable using transmission electron microscope (Kim *et al.*, 2011), cause local cracking of the polymer (Olea-Mejía *et al.*, 2012), and even sufficient morphological instabilities to severely deform the geometry FIB-prototyped nanostructures (Schmied *et al.*, 2012, 2014; Orthacker *et al.*, 2014). For pure polymers the thermal damage localized to the ion beam impact area can be minimized using cryogenic cooling, low current milling and smart navigation of the ion beam (Kim *et al.*, 2011, Bassim *et al.*, 2012, Lee *et al.*, 2012, Olea-Mejía *et al.*, 2012, Schmied *et al.*, 2012, 2014, Orthacker *et al.*, 2014). In the latter approach the ion beam exposure pattern is altered from the common pixelated line-by-line raster to increase the time in-between re-exposure of individual points. Increasing this so called loop time past an ion beam current and milled area dependent threshold reduces the maximum temperature rise by allowing for conductive dissipation of heat deposited by ion beam exposure.

In this work we used FIB-SEM to study internal morphology of single component polysiloxane corrosion barrier coatings with and without haze grey pigment additives. These novel coatings are potential candidates for replacing silicone alkyds currently used to cover topsides of naval surface vessels. The polysiloxane coatings are hydrophobic and have enhanced hardness, colour-stability, gloss retention, and cleanability as compared to the silicone alkyds (Iezzi, 2012; Iezzi *et al.*, 2013). We show that the pure polysiloxane paint can be FIB cross sectioned at room temperature with a wide range of ion beam currents (1–20 nA) without introducing any major geometrical alterations to the exposed section. In contrast, we observed an unexpected mode of severe damage that occurs during FIB milling of the pigmented polysiloxane coating with ion beam current higher than 1 nA. Specifically, we report that FIB milling of such composites can lead to formation of multiple voids within the substrate as far as 5 μm away from the ion beam impact. We use experiments and modelling to identify the physical mechanisms responsible for formation of the voids and FIB milling conditions that mitigate these severe artefacts.

Materials and methods

Polysiloxane coating synthesis, preparation, and characterization

The resin with approximate chemical formula $C_{52}H_{107}N_9O_{15}Si_3$ was synthesized by reacting N-butyl-3-aminopropyltrimethoxysilane with a homopolymer of hexamethylene diisocyanate, at a 1:1 molar ratio, at 50°C in aromatic naphtha solvent until all isocyanate has been consumed (Iezzi, 2012). After the clear polymer was synthesized, a haze grey colouring was achieved by dispersing colorizing pigments (titanium oxide, chromium green-black hematite, and yellow iron oxide) using a high-speed mixer. Solvents were added to adjust the viscosity, followed by a catalyst (e.g. dibutyltin dilaurate). Addition of the pigment particles decreased the static contact angle water from 102.4° ± 1.4° for the clear to 94.0° ± 1.4° for haze grey coatings. Similarly, the advancing and receding water contact angles changed from 106.8° ± 0.4° and 74.0° ± 3.2° to 95.4° ± 1.8° and 46.6° ± 1.7°, respectively.

For the imaging and milling experiments, several drops of clear and pigmented polymer were deposited on separate mirror polished 2.5 cm diameter aluminum SEM stubs (Ted Pella Inc., Redding, CA, USA). The drops were allowed to cure at 22–24°C with 30–50% relative humidity for at least one week. Optical images of the drops were taken using an Axio-Zoom V16 microscope (Zeiss, Peabody, MA, USA) with Apo 1.5x lens. The energy dispersive x-ray (EDS) spectra of the samples were collected for 600 s using an Apollo detector with Genesis software (EDAX, Mahwah, NJ, USA) mounted onto an Amray 1910 SEM (Semtech Solutions, North Billerica, MA, USA) with an electron beam energy of 15 keV and condenser lens setting of –20. Prior to FIB-SEM milling and imaging, samples were coated with a thin gold-palladium layer using a 208 HR Sputter Coater (Cressington, Wadford, UK).

Differential scanning calorimetry and thermogravimetric analysis

Flakes of the cured clear polysiloxane were frozen using liquid nitrogen and manually ground using a mortar and pestle. About 5 mg of the powder was inserted into an aluminium crucible that was placed on the balance arm of a Mettler-Toledo STAR^e TGA/DSC 1 (Greifensee, Switzerland). Prior to closing of the crucible and the furnace, a 1-min-long nitrogen gas purging step was performed at a flow rate of 20 mL min^{-1}. During the experiment the nitrogen gas flow was increased to 50 mL min^{-1}. The furnace was heated at a rate of 2°C min^{-1} from room temperature to 550°C, and held at this temperature for three hours prior to cooling back to room temperature. The presence of residual black powder was visually confirmed. The STAR^e evaluation software was used to integrate the DSC curve between 138 and 330 min to obtain the total heat transfer. To calculate the specific enthalpy of decomposition, the integrated value was divided by the decreased mass of the sample after residual solvent evaporation that occurred around 150°C (4.5 mg).

Thermal conductivity measurement

The thermal conductivity of polysiloxane was measured using the 3ω method (Cahill, 1990). To prepare samples for measurement, Al metal lines were deposited on a clear film of cured polysiloxane on silicon wafer using photolithography. The lines were 10 μm wide, 1.0 mm long, and 150 nm thick. These lines functioned as both the heat source and thermometer. During the measurements, an alternating current was run through the Al line at a series of frequencies and the corresponding third harmonic of the voltage response was measured using SR830 lock-in amplifier (Stanford Research Systems, Sunnyvale, CA, USA). To convert the electrical signals into thermal responses, the temperature coefficient of resistance of 3ω lines were measured using a home-built thermal stage.

FIB-SEM

The experiments were conducted using a Nova 200 FIB-SEM (FEI Co, Hillsboro, OR, USA) with Ga$^+$ column and field emission electron gun. The SEM imaging was performed with electron beam energy of 5 keV and current of 0.4 nA with a per point dwell time between 0.3 and 3 μs. All FIB processing steps were performed with an ion beam energy of 30 keV. Prior to FIB milling, an approximately 0.5 μm thick and 5 μm by 15 μm protective platinum film was deposited using FIB induced deposition of the organometallic gas with an ion beam current of 0.3 nA. FIB milling was performed with an ion beam current between 0.5 and 20 nA with a per point dwell time of 1 μs and a 50% overlap between consecutive points. Large 10 μm by 15 μm cuts with a staircase geometry and maximal depth of about 7 μm were performed using the 'regular cross section' mode with ion beam currents ranging from 1 to 20 nA. Polishing of the exposed cross sections was performed with an ion beam current of 0.5–1 nA using the 'cleaning cross section' mode. Occasional secondary electron images from the 'FIB view' were captured with a dwell time of 100 ns and a raster size of 512 by 471 pixels. To determine the FIB sputtering rate of the clear polymer, 5 μm by 5 μm squares were milled for 6, 12, 25, 50 and 75 s with ion beam currents of 3 and 7 nA. The FIB sputtering rate was determined from a linear fit to average depth measurements taken at each exposure time (six depth measurements per point). The calculated sputtering rate was 0.98 μm^3 s^{-1} (0.33 μm^3 nC^{-1}) and 1.9 μm^3 s^{-1} (0.27 μm^3 nC^{-1}) for 3 and 7 nA cuts, respectively. All experiments were conducted with sample located at the eucentric position with a working distance of 5.3 mm and 52° tilt.

Results

Figure 1 illustrates a typical three step FIB-SEM cross sectioning procedure consisting of: (1) localized deposition of a protective film through ion or electron beam induced deposition of carbon or carbon-platinum composite, (2) high ion beam current removal of a large material volume and (3) low ion beam current polishing of the exposed vertical cross section. The ~0.5 to 1-μm-thick protective cap is deposited to minimize milling nonuniformities that can cause formation of a jagged cross section (displayed through vertical curtain-like stripes on SEM image). During the second step a large volume of the sample with a rectangular base is removed. The milling time during this step is reduced by removing only a wedge-like or staircase-like volume that is directly blocking the electron beam access to the cross section of interest. To further reduce the milling time, as high as practically possible ion beam current is used during this step. However, fast milling with ion beam currents on the order of a few nanoamps, and with that beam diameter of ~50 to 500 nm, typically results in a crude cut quality and masking of the actual cross section face underneath a layer of redeposited material (e.g. see SEM image in Fig. 1B). In the third "cleaning" step, ion beam with a current below 1 nA and diameter of below 50 nm is used to 'polish' the cross section. Comparison of the before and after 'cleaning step' SEM images of the cross section in Figures 1(B) and (C) clearly shows that FIB polishing exposes the particles hidden underneath the redeposited material.

We used the above FIB-SEM procedure to study internal morphology of single component polysiloxane coatings without (i.e. clear) and with haze grey pigment additives (see optical images in Figs. 2A and B). To be qualified for application to navy ships, the organic coating must have a number of particulate additives that serve various functions ranging from haze grey colouring to minimizing thermal loads by reducing solar absorbance (MIL-PRF-24635E, 2009). The energy dispersive x-ray spectra (EDS) of the clear and haze grey samples shown in Figures 2(A) and (B) illustrate this point. In addition to strong carbon, silicon, oxygen, aluminium (from substrate) peaks present in both spectra, the haze grey coating spectrum includes titanium, iron, and chrome peaks corresponding to titanium oxide, chromium green-black hematite and yellow iron oxide pigments. The images in Figures 2(C) and (D) show pure polysiloxane polymer after a 15 μm wide and ~7 μm deep cross section was exposed using FIB milling at 1 and 7 nA, respectively. While milling at the lower current produced a better defined geometry (i.e. the staircase pattern and vertical side-walls), it took seven times longer than removal of same material volume at the higher current (20 min at 1 nA vs. 2:51 min at 7 nA). At this stage obtaining a high quality of the milled ditch geometry is not critical since a low current cross section polishing step is required to clear away redoposited material. Consequently, performing the crude milling step of the clear sample at a current higher than 1 nA provides adequate results and is preferred because it reduces the overall milling time.

In contrast to the clear sample, we found that the morphology of the FIB milled pigmented composite sample was highly dependent on the ion beam current. The images in Figure 2(E) show that FIB milling of the composite sample at 1 nA with

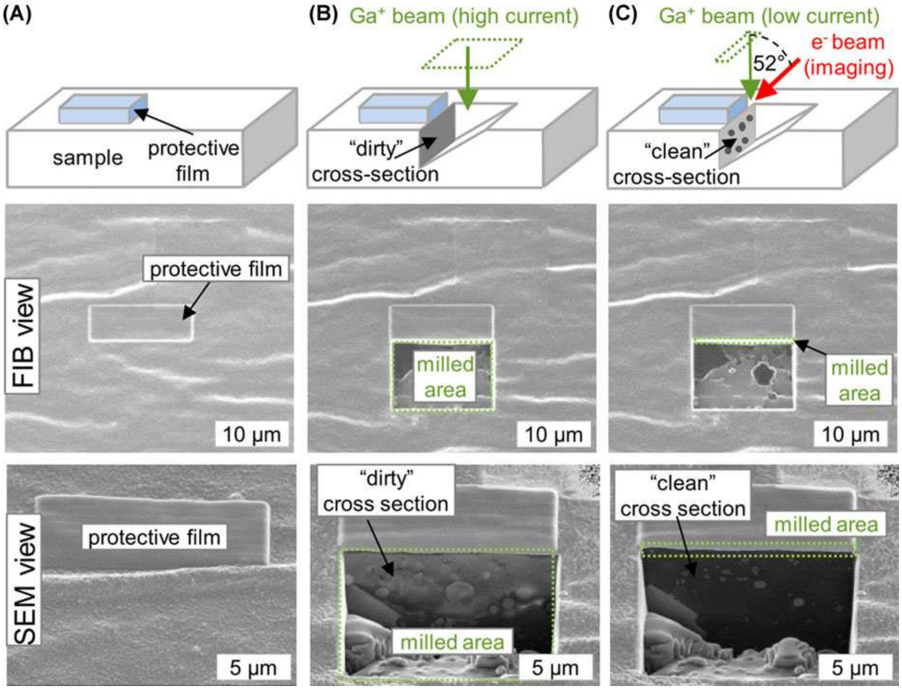

Fig. 1. Schematics and representative FIB-view and SEM-view images illustrating typical FIB-SEM cross sectioning procedure consisting of (A) protective film deposition, (B) high ion beam current removal of a large material wedge and (C) low ion beam current polishing to expose a clean cross section from underneath redeposited material. To facilitate interpretation of the schematics, the sample is oriented horizontally instead of at 52° tilt used in experiments.

a 0.5 nA polishing step produced a smooth cross section with clearly visible pigment particles. Since the polymer is sputtered away at a higher rate than the mostly ceramic particles ($\sim 0.3\ \mu m^3\ nC^{-1}$ for polysiloxane vs. $0.15\ \mu m^3\ nC^{-1}$ TiO_2), several pigment particles rise above the polymer on the bottom of the milled ditch. Besides the partially milled particles, deep holes also formed on the bottom of the ditched milled at 7 nA. The images in Figure 2(F) show that in addition to the holes on the bottom, a number of voids with size ranging from ~0.2 to 3 μm also formed on the vertical cross section. We observed formation of the voids during milling of the pigmented sample at any ion beam current above 1 nA (up to 20 nA).

We used the procedure illustrated in Figure 2(G) to confirm that these voids are indeed caused by high current ion beam milling. Specifically, we first milled staircase-like shapes with rectangular base of 15 by 10 μm and maximum depth of ~7 μm at currents of 1, 3, 5, 7 and 20 nA. Subsequently, we progressively milled into the material covered by the protective cap at 1 nA, moving away from the edge of the original crude cut in 1 μm thick, 15 μm wide, and ~7 μm deep slices. The images of the revealed cross sections in Figure 2(G) show that for the 5 nA crude cut voids are present until the third slice (i.e. the image of the cross section taken after the fourth slice is void free). We used this procedure to determine void penetration depth away from the impact of the high energy ion beam during the crude milling step. We found that the penetration depth scaled with the current, being 2, 3, 4 and 5 μm for ion beam currents of 3, 5, 7 and 20 nA, respectively. We point out that in all the cases voids were present within material volume that was not directly exposed to the high current beam. Consequently, in contrast to holes on the bottom of the milled ditch, the observed voids could not have been caused by the large difference between the polymer and particle milling rates. In the next section we propose and discuss an alternative thermal mechanism that leads to formation of the voids.

Discussion

We propose that void formation occurs via ion beam heating of the pigment particles that subsequently leads to decomposition and vaporization of the surrounding polysiloxane. The schematic in Figure 3(A) illustrates that after decomposition of the polymer at the particle surface, voids can enlarge via vaporization of the solid in contact with the entrapped hot vapours. Since initially the created vapours will not have room to expand, their pressure will be significant. Consequently, voids could potentially expand through plastic deformation of the surrounding polymer. In addition, nonlocalized secondary voids could form through failure of weaker parts of the composite surrounding the original void (e.g. neighbouring particle-matrix interface) and vapour leakage.

The TGA and DSC results shown in Figure 3(B) indicate that four fifths of the total mass loss during polysiloxane

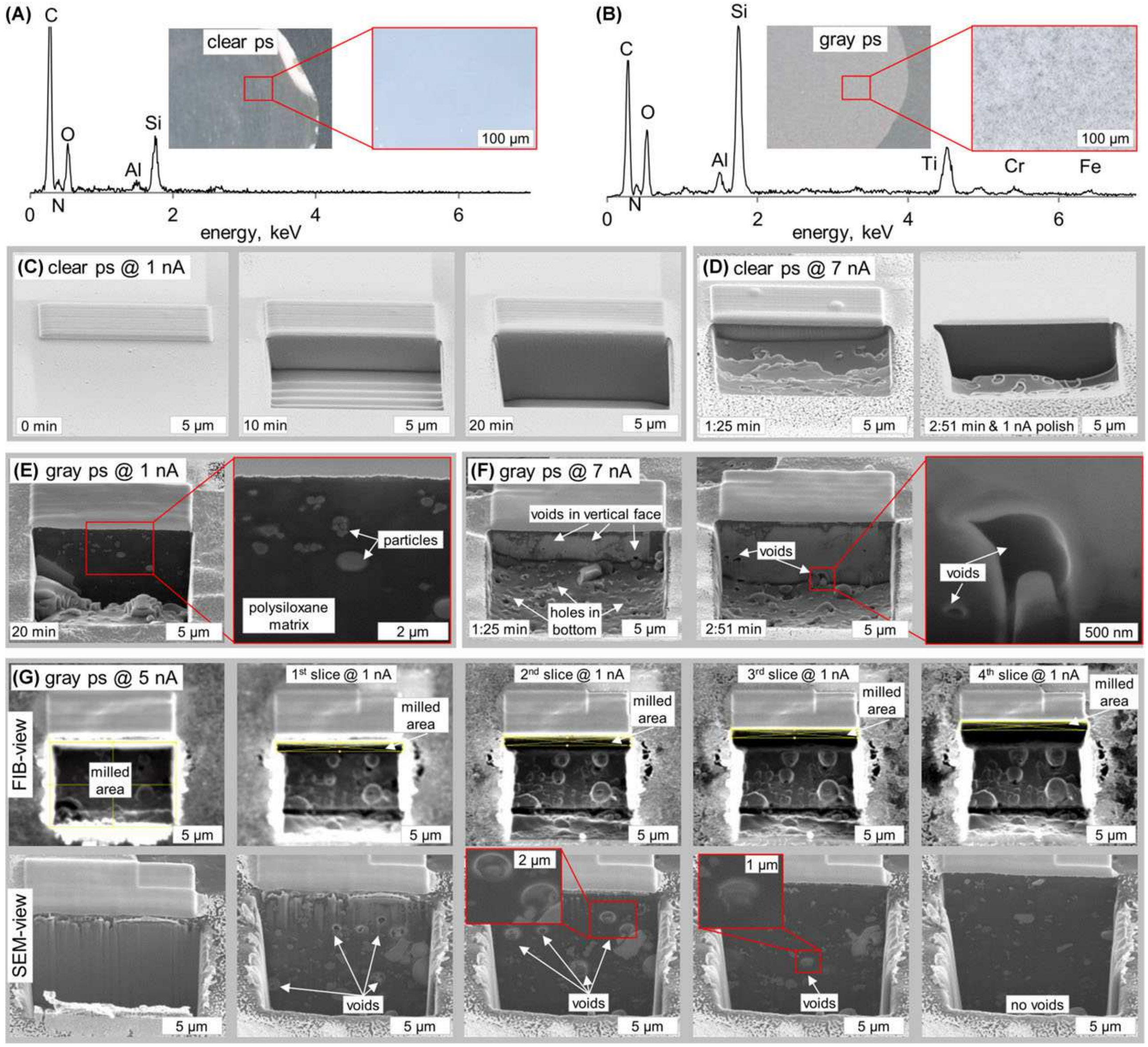

Fig. 2. EDS spectra and optical images of (A) clear and (B) haze grey pigmented polysiloxane (ps); (C) to (F) 52° tilt SEM images of clear polysiloxane FIB milled at (C) 1 nA and (D) 7 nA and of the haze grey polysiloxane FIB milled at (E) 1 nA and (F) 7 nA; (G) corresponding FIB-view and SEM-view images of sequential slicing away from the original cut face to determine the void penetration depth.

decomposition occurs between $\sim$350°C and $\sim$550°C. This step involves breaking down of the polymer into solid fumed silica and black carbon as well as gases including water, carbon dioxide, and hydrocarbons. The other one fifth of the total lost mass occurred at temperature lower than $\sim$150°C. Since this low temperature mass loss is not associated with an endothermic peak, it likely is caused by outgassing of residual volatile organic compounds and solvents. In contrast, the predominant titanium oxide pigment is much more thermally stable with melting and vaporization temperatures of 1843°C and 2972°C, respectively. Thus, if the ion beam can heat the titanium oxide particles to 350°C, polysiloxane at the particle surface could be vaporized with further ion beam exposure.

Since the pigment particles have size, d_p, comparable to or greater than the ion beam diameter (d_b defined as full width at half maximum of the assumed Gaussian beam distribution), ion beam heating cannot be evaluated in terms of effective thermal conductivity. In fact, such analysis would lead to an incorrect conclusion that the presence of the particles, whose addition increases the effective thermal conductivity of the composite ($\sim$11 W Km^{-1} for TiO$_2$ vs. 0.19 ± 0.02 W Km^{-1} for polysiloxane), would decrease the maximum temperature rise ($\Delta T \sim 1/k$). Based on simulations performed using SRIM

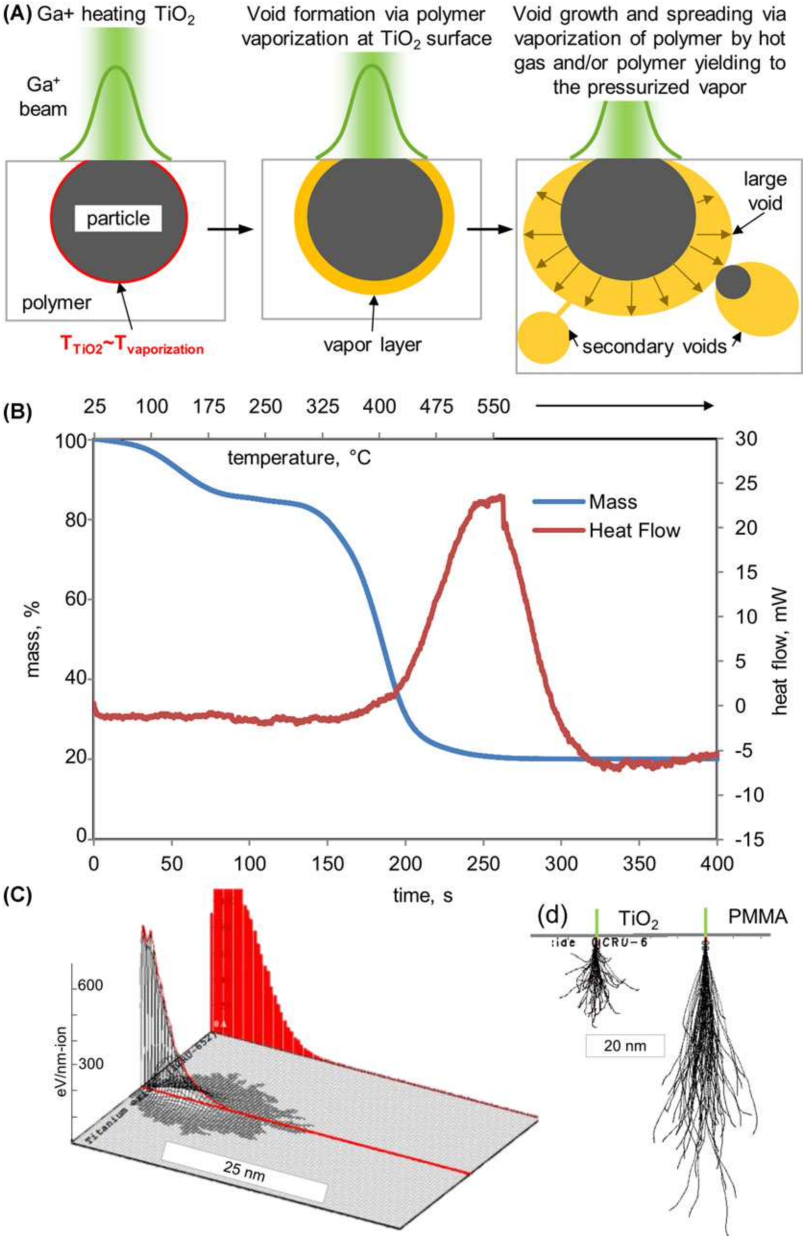

Fig. 3. (A) Schematic of the proposed thermal route of void formation ($T_{vaporization}$ stands for vaporization temperature of polysiloxane) (B) TGA and DSC plots showing mass loss and heat flow during decomposition of the clear polysiloxane, (C) distribution of phonons created by 30 keV Ga+ ions scattering within TiO_2 and (D) corresponding projection of 100 ion scattering tracks in TiO_2. Ion scattering tracts in Poly(methyl methacrylate) (PMMA) are also shown for comparative purposes.

software (Ziegler & Biersack, 2012), about two thirds of the total energy of Ga^+ ions (E_t= 30 keV) scattering in TiO_2 is lost in inelastic collisions with the substrate's atoms. Through recoil of the atoms after the collisions, the energy lost by the ion generates phonons (Schmied *et al.*, 2014). The plots of SRIM simulations in Figures 3(C) and (D) show that majority of the ion scattering events and phonon generation occurs within about ~20 nm of the surface. Since the smallest pigment particles have a significantly larger size of 100 to 200 nm, the ion beam with current i can be approximated as a surface heat source with diameter d_b and power $\dot{q} = 2iE_t/3$.

To estimate the temperature increase of a pigment particle due to this heat source, we assume that the temperature gradient within the particle is negligible (i.e. lumped thermal mass model). This assumption is reasonable as the time scale for heat conduction across the particle, t_{con}, is much shorter than the per pointion beam dwell time, t_{dwell}. Whereas t_{dwell} is approximately 1 μs, t_{con} ranges from 2.5 to 70 ns for d_p

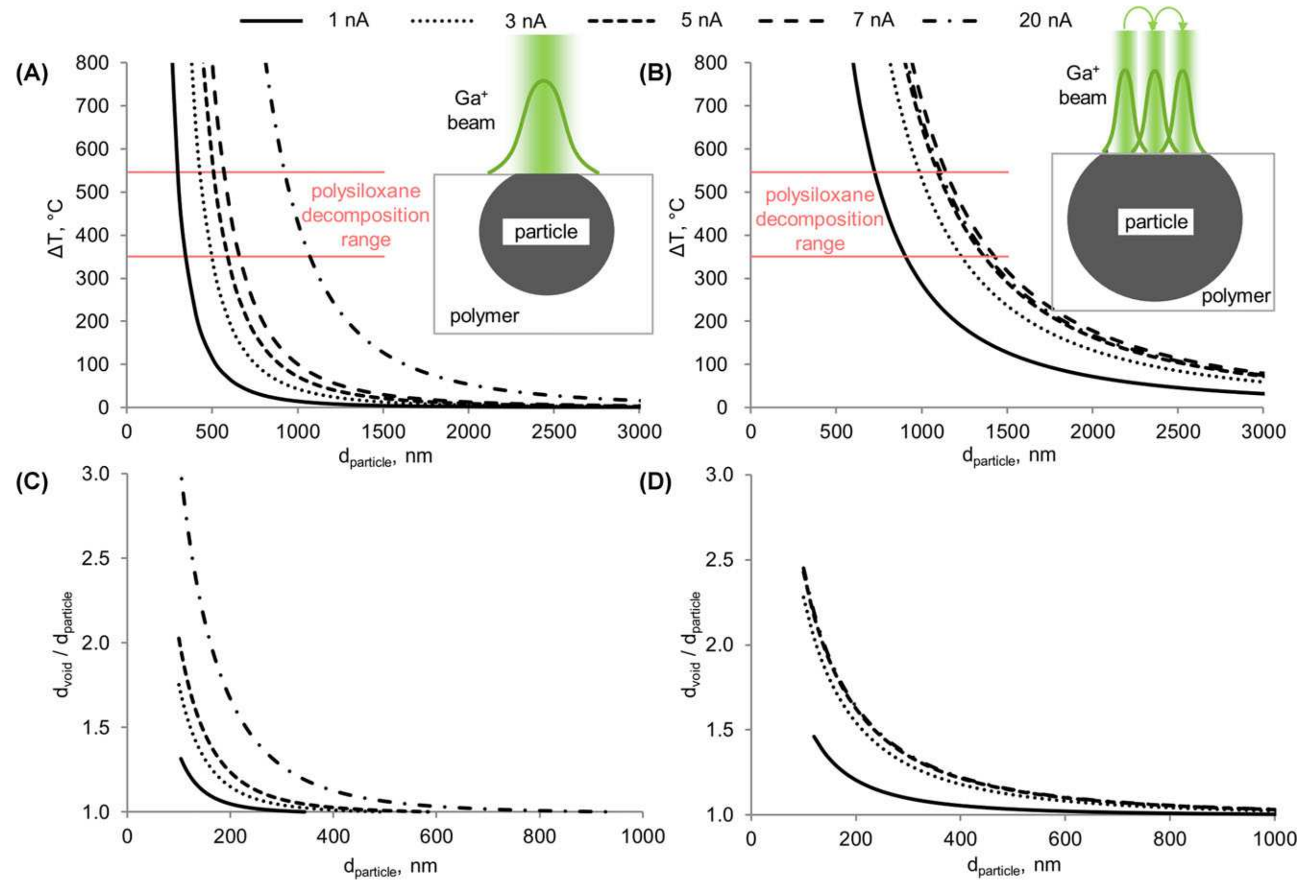

Fig. 4. Plots of calculated temperature increase of spherical titanium oxide particles with varied diameters due to (A) single and (B) multiple consecutive exposures to 30 keV Ga$^+$ beam with current in the range of 1–20 nA; (C) and (D) corresponding relative diameter of voids (d_{void}) that could be created around the particles ($d_{particle}$) heated to 350°C with remaining energy deposited by the ion beam exposure.

ranging from 100 to 1000 nm ($t_{con} \sim \frac{d_p^2}{\alpha_p}$ where α_p is the TiO$_2$ particle thermal diffusivity, 4.4×10^{-6} m^{2}s^{-1}). Furthermore, because our measurement showed that the thermal conductivity of the polymer is two orders smaller than that of the TiO$_2$, we assume that the particle is thermally insulated. With these assumptions, the temperature increase due to single ion beam exposure can be estimated as $\Delta T_{single} \sim 6\dot{q}\,t_{dwell}/\pi\rho c_p d_p^3$ (ρ_p and c_p are the density and the gravimetric specific heat of TiO$_2$). This expression can also be modified to take into account cases when $d_p > d_b$ and the particle is exposed multiple times to the ion beam within the same raster loop (see schematics in Figs. 4A and B). Since the time in-between the exposure points is negligible comparing to the per point dwell time and the particle is treated as a lumped thermal mass, multiple consecutive exposures are equivalent to a single longer exposure. With the typical consecutive point separation distance of $d_b/2$, the temperature rise of an insulated particle due to multiple sequential ion beam exposures can be estimated as $\Delta T_{mult} \sim 6\dot{q}\,t_{dwell}(2d_p/d_b)/\pi d_p^3\rho c_p$. The plots in Figures 4(A) and (B) show that the pigment particles can reach the threshold temperature for polysiloxane decomposition (~350°C) after both single and multiple exposures to the ion beam. Particles with diameters below ~350 and ~1100 nm reach this temperature after single 1 μs exposure to 1 and 20 nA ion beam, respectively. If sequentially exposed $2d_p/d_b$ times for 1 μs to the 1 and 20 nA ion beam, particles smaller than ~950 and ~1500 nm will reach the threshold decomposition temperature, respectively.

Once the surface of the pigment particles is heated to the threshold decomposition temperature, a significant portion of energy imparted by ion beam during remaining exposure time will contribute to decomposition of the surrounding polymer. After the solid layer directly in contact with the particle is decomposed and partially vaporized, the surrounding polymer will be heated and decomposed by the created gases that, in turn, will be reheated by the particle. To roughly estimate size of voids that would form in the process, we assume that all energy imparted by the ion beam after particles reach ~350°C, $E_l = E_t - \Delta T\,\rho_p c_p \pi d_p^3/6$, leads to decomposition and vaporization of the polymer. In other terms, we assume that $E_l = \rho_{ps}\,V_{ps}\lambda_{ps}$, where ρ_{ps}, V_{ps}, and λ_{ps} are the density, volume, and specific enthalpy of decomposition of the polysiloxane.

To calculate the value of λ_{ps} we estimated the energy that was required to decompose our sample by integrating the DSC data under the endothermic peak (see Fig. 3B). By dividing this value by the sample mass, we obtained $\lambda_{ps} \sim 26$ kJ g^{-1}, which is in the range expected for high temperature polymers (Walters *et al.*, 2000). Assuming a spherical shape of the forming void, we can estimate its diameter as $d_{void} = \sqrt[3]{6E_l/\pi\rho_{ps}\lambda_{ps} + d_p^3}$. The plots in Figures 4(C) and (D) show that the relative diameter of the voids (d_{void}/d_p) increases with decreasing particle size. Exposure of particles with $d_p \sim 100$ to 200 nm to ion beam with current of 3 nA and higher can easily create voids with $d_{void}/d_p \sim 2$ to 3. In turn, a 1 nA ion beam can at most create spherical voids with $d_{void}/d_p \sim 1.5$. For the $d_p \sim 100$ nm, this corresponds to a nearly negligible ~25-nm-thick shell-like void around the particle. Since our simple model neglected any heat losses due to conduction and radiation, the actual void size is likely to be even smaller. Thus, our simple theoretical predictions agree well with our experiments and show that primary void formation occurs due to decomposition and vaporization of the polysiloxane around ~100 to 300 nm pigment particles exposed to 30 keV Ga$^+$ ion beam with $i \geq 3$ nA. We also note that the created vapors are confined within the volume previously occupied by the solid. Consequently, their pressure can rise dramatically. For example, water, which is one of the expected decomposition products, needs to be pressurized to ~100 MPa to have density near that of the polymer (~1 g cm^{-3}) at ~350°C (Lide, 2004). This value is comparable to both compressive and tensile yield strength of most polymers (MatWeb, 2014), implying that voids could also enlarge because the vapour exerts sufficient pressure to permanent deform the polymer. Similarly, secondary voids could be formed through microscopic cracking and leakage of the high pressure gases along mechanically weaker parts of the matrix such as neighbouring particle–polymer interfaces.

Conclusion

In this work we reported unexpected nonlocalized artefacts that occur during FIB milling of polysiloxane barrier coatings with pigment particles. Specifically, we showed that FIB milling of these samples at currents higher than 1 nA leads to formation of multiple microscopic voids within the sample. The void penetration depth increased proportionally to the ion beam current, reaching a maximum of 5 μm from the ion beam impact point for a current of 20 nA. In contrast, we did not observe formation of any voids in the clear polymer without the pigment particles even during FIB milling with current of 20 nA. Ion beam heating of the clear sample likely does decompose the polymer in the vicinity of the beam impact, however, the vapours are created at the surface and can easily escape.

By treating the pigment particle as an insulated lumped thermal mass, we showed that a single 1 μs exposure to a 1 and 20 nA ion beam can heat particles with diameters below ~350 and ~1100 nm to the threshold temperature for polysiloxane decomposition (~350°C). If sequentially exposed $2d_p/d_b$ times to 1 μs long 1 and 20 nA ion beams, particles smaller than ~950 nm and ~1500 nm will reach this temperature, respectively. By assuming that all energy imparted by the ion beam after the particles reaches ~350°C leads to decomposition and vaporization of the polymer, we showed that exposure of particles with diameters of 100–200 nm to ion beam with current of 3 nA and higher can easily create spherical voids with $d_{void}/d_p \sim 2$ to 3. In contrast, the model predicted that particle exposure to 1 nA ion beam would create negligibly small voids. These theoretical predictions agreed well with our experimental observations, corroborating our hypothesis that primary void formation occurs due to decomposition and vaporization of the polysiloxane around ion beam heated particles. We suspect that primary void enlargement and formation of secondary voids occurs due to mechanical damage of the polymer induced by the entrapped vapours that could be pressurized up to ~100 MPa. We note that severity of the ion beam heating problem could increase with milling of smaller sections, thus to avoid temperature increase past the decomposition threshold a lower current might be necessary.

Our work demonstrates that processes occurring during FIB-milling of pure polymers and their composites with strongly heterogeneous thermal and mechanical properties can differ dramatically. Strong damage to the composites can occur through unexpected mechanisms such as the one described in this work even at conditions that do not degrade the pure polymer. Thus, care must be taken during FIB-characterization of such composites to avoid confusion of processing induced artefacts and genuine features. This is particularly relevant to FIB-milling of corrosion barrier coatings, since one of the primary reasons for their characterization is quantification of the nanoscale porosity of pristine and weathered samples.

Acknowledgements

K.R., K.N.S. and L.P.W. acknowledge funding from US Department of Defense under Technical Corrosion Collaboration Program administered by the US Air Force Academy through grant no. FA7000-14-2-0015. K.R. also acknowledges startup funding from Ira A. Fulton Schools of Engineering at Arizona State University. R.W. and M.L. acknowledge funding support from the National Science Foundation through Grant no. CBET-1236656. Authors gratefully acknowledge the use of facilities at the LeRoy Eyring Center for Solid State Science at Arizona State University.

References

Aubry, C., Trigaud, T., Moliton, J.P. & Chiron, D. (2002) Polymer gratings achieved by focused ion beam. *Synthet. Metals* **127**, 307–311.

Bassim, N., Scott, K. & Giannuzzi, L.A. (2014) Recent advances in focused ion beam technology and applications. *MRS Bull.* **39**, 317–325.

Bassim, N.D., De Gregorio, B.T., Kilcoyne, A.L.D., Scott, K., Chou, T., Wirick, S., Cody, G. & Stroud, R.M. (2012) Minimizing damage during FIB sample preparation of soft materials. *J. Microsc.* **245**, 288–301.

Beach, E., Keefe, M., Heeschen, W. & Rothe, D. (2005) Cross-sectional analysis of hollow latex particles by focused ion beam–scanning electron microscopy. *Polymer* **46**, 11195–11197.

Bierwagen, G., Tallman, D., Li, J., He, L. & Jeffcoate, C. (2003) EIS studies of coated metals in accelerated exposure. *Prog. Organic Coat.* **46**, 149–158.

Brostow, W., Gorman, B.P. & Olea-Mejia, O. (2007) Focused ion beam milling and scanning electron microscopy characterization of polymer+ metal hybrids. *Mater. Lett.* **61**, 1333–1336.

Brunner, S., Gasser, P., Simmler, H. & Wakili, K.G. (2006) Investigation of multilayered aluminium-coated polymer laminates by focused ion beam (FIB) etching. *Surf. Coat. Technol.* **200**, 5908–5914.

Brunner, S., Tharian, P.J., Simmler, H. & Ghazi Wakili, K. (2008) Focused ion beam (FIB) etching to investigate aluminium-coated polymer laminates subjected to heat and moisture loads. *Surf. Coat. Technol.*, **202**, 6054–6063.

Cahill, D.G. (1990) Thermal conductivity measurement from 30 to 750 K: the 3ω method. *Rev. Scient. Instrum.* **61**, 802–808.

Chen, B., Guizar-Sicairos, M., Xiong, G. *et al.* (2013) Three-dimensional structure analysis and percolation properties of a barrier marine coating. *Scientific Rep.* **3**, 1177.

Chen, B., Hashimoto, T., Vergeer, F., Burgess, A., Thompson, G. & Robinson, I. (2014) Three-dimensional analysis of the spatial distribution of iron oxide particles in a decorative coating by electron microscopic imaging. *Prog. Organic Coat.* **77**, 1069–1072.

Das, K., Freund, J.B. & Johnson, H.T. (2015) Mechanisms of material removal and mass transport in focused ion beam nanopore formation. *J. Appl. Phys.* **117**, 085304.

Doutre, M., Freeman, A., Diak, B., Murray, A., Bevan, G. & Fuster-López, L. (2014) Fine pore structure characterization in two gessoes using focused ion bean scanning. In *MRS Proceedings*. Cambridge Univ Press.

Firpo, G., Angeli, E., Repetto, L. & Valbusa, U. (2015) Permeability thickness dependence of polydimethylsiloxane (PDMS) membranes. *J. Membr. Sci.* **481**, 1–8.

Iezzi, E., Martin, J., Tagert, J., Slebodnick, P., Wegand, J. & Lemieux, E. (2013) Single-component polysiloxane coating for navy topsides. 2013 Naval Research Laboratory Review.

Iezzi, E.B. (2012) Single-component coating having alkoxysilane-terminated N-substituted urea resins. US Patent US 8133964 B2.

Kato, M., Ito, T., Aoyama, Y., Sawa, K., Kaneko, T., Kawase, N. & Jinnai, H. (2007) Three-dimensional structural analysis of a block copolymer by scanning electron microscopy combined with a focused ion beam. *J. Polym. Sci. Part B: Polym. Phys.* **45**, 677–683.

Kawahara, S., Yamamoto, Y., Fujii, S., Isono, Y., Niihara, K.-I., Jinnai, H., Nishioka, H. & Takaoka, A. (2008) FIB-SEM and TEM observation of highly elastic rubbery material with nanomatrix structure. *Macromolecules*, **41**, 4510–4513.

Kim, S., Park, M.J., Balsara, N.P., Liu, G. & Minor, A.M. (2011) Minimization of focused ion beam damage in nanostructured polymer thin films. *Ultramicroscopy*, **111**, 191–199.

Lambourne, R. & Strivens, T. (1999) *Paint and Surface Coatings: Theory and Practice*, Elsevier, Cornwall, England.

Lee, C., Proust, G., Alici, G., Spinks, G. & Cairney, J.M. (2012) Three-dimensional nanofabrication of polystyrene by focused ion beam. *J. Microsc.*, **248**, 129–139.

Lide, D.R. (2004) *CRC Handbook of Chemistry and Physics*, CRC Press, New York.

Lin, J.-C., Heeschen, W., Reffner, J. & Hook, J. (2012) Three-dimensional characterization of pigment dispersion in dried paint films using focused ion beam–scanning electron microscopy. *Microsc. Microanal.* **18**, 266–271.

Linossier, I., Gaillard, F., Romand, M. & Feller, J. (1997) Measuring water diffusion in polymer films on the substrate by internal reflection Fourier transform infrared spectroscopy. *J. Appl. Polym. Sci.* **66**, 2465–2473.

Lins, A., Giannuzzi, L.A., Stevie, F.A., Price, B., Tucker, M. & Gutman, N. (2002) FIB/TEM analysis of paint layers from Thomas Eakins' The Crucifixion, 1880. In *Proceedings of the Materials Issues in Art and Archaeology VI: Symposium.* November 26–30, 2001, Boston, Massachusetts, USA. Materials Research Society.

Loos, J., van Duren, J.K., Morrissey, F. & Janssen, R.A. (2002) The use of the focused ion beam technique to prepare cross-sectional transmission electron microscopy specimen of polymer solar cells deposited on glass. *Polymer* **43**, 7493–7496.

Martínez, E., Engel, E., López-Iglesias, C., Mills, C.A., Planell, J.A. & Samitier, J. (2008) Focused ion beam/scanning electron microscopy characterization of cell behavior on polymer micro-/nanopatterned substrates: a study of cell–substrate interactions. *Micron* **39**, 111–116.

MatWeb, L. (2014) Material Property Data. MatWeb,[Online]. Available: http://www.matweb.com

MIL-PRF-24635E (2009) Performance Specification. Coating Systems, Weather-Resistant, Exterior Use.

Nguyen, T., Bentz, D. & Byrd, E. (1995) Method for measuring water diffusion in a coating applied to a substrate. *J. Coat. Technol.* **67**, 37–46.

Nguyen, T., Hubbard, J. & Pommersheim, J. (1996) Unified model for the degradation of organic coatings on steel in a neutral electrolyte. *J. Coat. Technol.* **68**, 45–56.

Niihara, K.-I., Kaneko, T., Suzuki, T., Sato, Y., Nishioka, H., Nishikawa, Y., Nishi, T. & Jinnai, H. (2005) Nanoprocessing and nanofabrication of a structured polymer film by the focused-ion-beam technique. *Macromolecules*, **38**, 3048–3050.

Olea-Mejía, O., Olea-Cardoso, O. & Lopez-Castañares, R. (2012) FIB-SEM combination technique for characterization of polymer composites. In *Current Microscopy Contributions to Advances in Science and Technology* (ed. by A. Mendez-Vilas), pp. 1060–1065. Formatex Research Center, Badajoz, Spain.

Orthacker, A., Schmied, R., Chernev, B., Fröch, J., Winkler, R., Hobisch, J., Trimmel, G. & Plank, H. (2014) Chemical degradation and morphological instabilities during focused ion beam prototyping of polymers. *Phys. Chem. Chem. Phys.* **16**, 1658–1666.

Qin, L., Mergos, I.A. & Verweij, H. (2015) Obtaining accurate cross-section images of supported polymeric and inorganic membrane structures. *J. Membr. Sci.* **476**, 194–199.

Schmied, R., Chernev, B., Trimmel, G. & Plank, H. (2012) New possibilities for soft matter applications: eliminating technically induced thermal stress during FIB processing. *RSC Adv.* **2**, 6932–6938.

Schmied, R., Froch, J.E., Orthacker, A., Hobisch, J., Trimmel, G. & Plank, H. (2014) A combined approach to predict spatial temperature evolution and its consequences during FIB processing of soft matter. *Phys. Chem. Chem. Phys.* **16**, 6153–6158.

Stevie, F., Giannuzzi, L. & Prenitzer, B. (2005) *Introduction to Focused Ion Beams: Instrumentation, Theory, Techniques and Practice*. Springer, New York.

Van der Wel, G. & Adan, O. (1999) Moisture in organic coatings—a review. *Prog. Organic Coat.*, **37**, 1–14.

Vineyard, G. (1976) Thermal spikes and activated processes. *Radiat. Effects*, **29**, 245–248.

Volkert, C.A. & Minor, A.M. (2007) Focused ion beam microscopy and micromachining. *MRS Bull.*, **32**, 389–399.

Walters, R.N., Hackett, S.M. & Lyon, R.E. (2000) Heats of combustion of high temperature polymers. *Fire Mater.*, **24**, 245–252.

White, H., Pu, Y., Rafailovich, M. *et al*. (2001) Focused ion beam/lift-out transmission electron microscopy cross sections of block copolymer films ordered on silicon substrates. *Polymer*, **42**, 1613–1619.

Wong, K., Haslauer, C., Anantharamaiah, N., Pourdeyhimi, B., Batchelor, A. & Griffis, D. (2010) Focused ion beam characterization of bicomponent polymer fibers. *Microsc. Microanal.*, **16**, 282–290.

Ziegler, J.F. & Biersack, J.P. (2012) *SRIM: The Stopping and Range of Ions in Matter*. Chester, MD.